Title
A method for the topographical identification and quantification of high frequency oscillations in intracranial electroencephalography recordings.

Permalink
https://escholarship.org/uc/item/0t64n7k9

Authors
Waldman, Zachary J
Shimamoto, Shoichi
Song, Inkyung
et al.

Publication Date
2018

Peer reviewed

A method for the topographical identification and quantification of high frequency oscillations in intracranial electroencephalography recordings

Zachary J. Waldman[a], **Shoichi Shimamoto**[a], **Inkyung Song**[a], **Iren Orosz**[b], **Anatol Bragin**[a], **Itzhak Fried**[d], **Jerome Engel Jr.**[c], **Richard Staba**[c], **Michael R. Sperling**[a], and **Shennan A. Weiss**[a,*]

[a]Department of Neurology, Jefferson Comprehensive Epilepsy Center, Thomas Jefferson University, Philadelphia, PA, USA

[b]Department of Radiology, David Geffen School of Medicine, University of California Los Angeles, Los Angeles, CA, USA

[c]Department of Neurology, David Geffen School of Medicine, University of California Los Angeles, Los Angeles, CA, USA

[d]Department of Neurosurgery, David Geffen School of Medicine, University of California Los Angeles, Los Angeles, CA, USA

Abstract

Objective—To develop a reliable software method using a topographic analysis of time-frequency plots to distinguish ripple (80–200 Hz) oscillations that are often associated with EEG sharp waves or spikes (RonS) from sinusoid-like waveforms that appear as ripples but correspond with digital filtering of sharp transients contained in the wide bandwidth EEG.

Methods—A custom algorithm distinguished true from false ripples in one second intracranial EEG (iEEG) recordings using wavelet convolution, identifying contours of isopower, and categorizing these contours into sets of open or closed loop groups. The spectral and temporal features of candidate groups were used to classify the ripple, and determine its duration, frequency, and power. Verification of detector accuracy was performed on the basis of simulations, and visual inspection of the original and band-pass filtered signals.

Results—The detector could distinguish simulated true from false ripple on spikes (RonS). Among 2934 visually verified trials of iEEG recordings and spectrograms exhibiting RonS the accuracy of the detector was 88.5% with a sensitivity of 81.8% and a specificity of 95.2%. The precision was 94.5% and the negative predictive value was 84.0% (N = 12). Among, 1,370 trials of iEEG recording exhibiting RonS that were reviewed blindly without spectrograms the accuracy of the detector was 68.0%, with kappa equal to 0.01 ± 0.03. The detector successfully distinguished

*Corresponding author at: Thomas Jefferson University, Department of Neurology and Neuroscience, Comprehensive Epilepsy Center, Principal Investigator: Computational Epilepsy Research Laboratory, 901 Walnut St., Suite 400, Philadelphia, PA 19107, USA. Fax: +1 215 503 3804. Shennan.Weiss@jefferson.edu (S.A. Weiss).

ripple from high spectral frequency 'fast ripple' oscillations (200–600 Hz), and characterize ripple duration and spectral frequency and power. The detector was confounded by brief bursts of gamma (30–80 Hz) activity in $7.31 \pm 6.09\%$ of trials, and in $30.2 \pm 14.4\%$ of the true RonS detections ripple duration was underestimated.

Conclusions—Characterizing the topographic features of a time-frequency plot generated by wavelet convolution is useful for distinguishing true oscillations from false oscillations generated by filter ringing.

Significance—Categorizing ripple oscillations and characterizing their properties can improve the clinical utility of the biomarker.

Keywords

High-frequency oscillation; Ripple; Filter ringing; Wavelet; Topography

1. Introduction

Up to one third of patients with focal seizures are medically refractory, and resective epilepsy surgery or responsive nerve stimulation (RNS) placement is required to reduce seizure burden or render the patient seizure free (Wiebe et al., 2001; Engel et al., 2012). High Frequency Oscillations (HFOs) consist of brief (<200 μsec) bursts of energy with a spectral content ranging between 80–600 Hz and have shown promise as a electrophysiological biomarker of epileptogenic brain tissue (Engel et al., 2009; Gotman, 2010; Jacobs et al., 2012). HFOs with a spectral content in the 80–250 Hz band are commonly referred to as ripples, while those in the 250–600 Hz band are termed fast ripples (Staba et al., 2002; Bragin et al., 2002). HFOs can be detected visually but this is arduous and time consuming (Zelmann et al., 2009), and inter-reader agreement can be poor (Gardner et al., 2007). To overcome these difficulties, there has been increasing interest in methods to automate the identification of HFOs from iEEG recordings (Jacobs et al., 2008; Zelmann et al., 2012; Birot et al., 2013; Burnos et al., 2014). A paradox intrinsic to the utilization of high-frequency oscillations for clinical purposes is that because inter-reader agreement is poor, it is challenging to validate automated detectors. Nevertheless, the results from the automated detectors can provide clinically useful information. One important area of investigation is defining classes of HFOs that may help improve inter-reader agreement.

In both manual and automated HFO detection, it is common practice to first apply a high pass filter to the continuous intracranial EEG (iEEG) or local field potential (LFP) recordings (Weiss et al., 2016a, 2016b). After high-pass filtering, HFOs can be observed visually or detected automatically as an increase in the signal amplitude above a threshold of 3–5 standard deviations of the mean for at least three oscillatory cycles (Csicsvari et al., 1999; Staba et al., 2002; Weiss et al., 2016b).

However, when sharp transients such as inter-ictal epileptiform spikes (IES) are band-pass filtered a sinusoid-like waveform resembling an HFO can result (Bénar et al., 2010). The energy spread over a continuous broad frequency range is due to how transients are

represented in the frequency space, because the Fourier transform of a Dirac impulse is a constant.

One strategy for distinguishing true HFOs from false HFOs is based on time-frequency analysis using wavelets (Liu et al., 2016). A wavelet convolution or transform of a sharp transient appears as a "candle" with a gradual and continuous taper in power with increasing frequency, while a true oscillation appears as a distinct "blob" of power in time-frequency coordinates (Benar et al., 2010; Birot et al., 2013).

We utilized the difference in the time-frequency representation of sharp transients and true high-frequency oscillations, to develop an automatic software method for classifying and quantifying ripples. Time-frequency maps of time series have an inherent topography defined by isopower contours. A true ripple is represented by a "blob" of power within the ripple band (80–200 Hz) and if contour lines are defined for a time-frequency representation of the "blob", with the maximum and minimum frequencies constrained to the ripple band, the contours will have closed loops. In contrast, a false ripple is represented by a "candle" of power in the ripple band, but importantly this "candle" extends below the ripple band. Therefore, when the contour lines are defined for the "candle" within the ripple band, the contours will have open loops. In the current study we tested whether the open-, or closed-loop properties of time-frequency plot contour lines could be used to differentiate true- and false- ripples on spikes i.e. epileptiform discharges, and whether analysis of the contour lines could be used to define ripple spectral content, power, and duration.

2. Methods

2.1. Patients

Recordings were selected from patients who underwent intracranial monitoring with depth electrodes between 2014 and 2016 at University of California Los Angeles (UCLA) for the purpose of localization of the seizure onset zone. The inclusion criteria were at least one night and day of intracranial recording with 2000 Hz sampling rate and at least 4 h of interictal EEG uninterrupted by seizures.

All clinical data from the patient's inpatient and postsurgical follow-up charts were provided. Patients underwent pre-surgical magnetic resonance imaging (MRI) and stereotactic electrode implantation, as well as a CT scan to localize electrode and a postsurgical MRI after the respective surgery. This study was approved by the UCLA institutional review board.

2.2. EEG recordings and segment selection

Clinical iEEG (0.1–600 Hz; 2000 samples per second; reference scalp Fz) was recorded from 7-contact depth electrodes using a Nihon-Kohden 256-channel JE-120 long-term monitoring system (Nihon-Kohden America, Foothill Ranch, CA, U.S.A.). The recordings were acquired during a 35–60 min epoch of mixed-stage sleep. Sleep was confirmed by video-EEG inspection revealing K-complexes, spindles, slow waves, and a paucity of muscle artifact. We did not perform concurrent electrooculography (EOG) and electromyography (EMG) recordings.

One-second trials of ripples occurring on inter-ictal discharges were identified using a previously described algorithm (Weiss et al., 2016b; Shimamoto et al., 2018). In brief, (1) INFOMAX independent component analysis (Bell and Sejnowski, 1997) was applied to referential recordings to reduce muscle contamination, and demarcate artefactual ripple events produced by muscle contamination (2) ripples were detected using a Hilbert detector applied to the band-pass filtered and ICA processed signal, (3) for each ripple detected a one-second trial was generated with a ripple centered at 0.5 s, (4) To distinguish ripples that occur during epileptiform spikes from all other ripples, we utilized a validated method (Shimamoto et al., 2018). We calculated the derivative of the peri-ripple band-pass filtered (4–30 Hz) iEEG and applied a threshold of 4 µV/msec. If the one second iEEG trials containing ripple events exceeded this threshold within ±50 ms that ripple was included for subsequent analysis. All the analysis in this study was performed using custom software written in Matlab 2016b (Natick, MA).

2.3. Wavelet convolution

A time-frequency analysis of the iEEG recording was performed using a wavelet convolution in the time domain (Dvorak and Fenton, 2014). Complex Morlet wavelets were created with constant frequency domain width $\frac{f_o}{\sigma_f} = 7$, Where f_o is the wavelet central frequency and σ_f is the standard deviation of its Gaussian envelope in the frequency domain. The central frequency, and the standard deviation of the Gaussian envelope values were frequency dependent and varied between the lower and upper limits of the TF analysis. The frequency bandwidth at a given frequency f_o is equal to $\frac{f_o}{7} * 2$. Prior to performing the wavelet convolution, the digital recording of the brain signal was padded with zeros until the sample count was equal to the closest power of two greater than the initial number of samples. The time frequency plot was not normalized.

Ripple events occur within a range of 80–200 Hz. Due to boundary effects caused by continuous wavelet convolution of finite-length signals, a range of 50–240 Hz was selected for the time-frequency (TF) plot in order to buffer the frequency range of interest. We also discarded the initial and final 45 ms of the time-frequency (TF) plot to further reduce boundary effects.

2.4. Topographical analysis of the time-frequency plot

The topographical analysis of the TF plot was performed by calculating a contour map consisting of 50 contours of isopower in the region of the TF plot centered on the candidate event, determined by the Hilbert detector, and including 100 ms prior to the event, and 100 ms after the event. Over the total range of power values in the TF plot, 50 contour levels were computed and scaled as equal data unit lengths. The method next identified all the vertices of each of the isolines of constant power in the TF map. Thus each contour was described by its power magnitude level, and the time/frequency coordinates of its vertices.

2.4.1. Defining groups of open- and closed- loop contours—Contours corresponding to power values less than a threshold defined by 0.2 * ((max$_{tf\text{-power}}$ −

min$_{tf-power}$) + min$_{tf-power}$ were removed. Each of the remaining contours was subsequently classified as a closed loop contour (CLC) if the contour's first and last vertex coordinate was identical, and an open loop contour (OLC) if the first and last vertex were distinct. Groups of CLCs, which either surround or are surrounded by other CLCs, were identified. If, in a group, the contour with the highest power level surrounded the other members of that group, the group was identified as a valley and removed from the time-frequency map. Groups containing fewer than 3 closed-loop contours were categorized as a 'lone contour group' and were removed from consideration. If one or more CLC groups remained, the candidate true ripple on spike event is identified as the group associated with the highest local maximum. In this study, all 1-s iEEG trials that were analyzed using the topographical approach were believed to contain either a ripple oscillation, and/or inter-ictal epileptiform discharge.

2.4.2. Quantifying ripple on spike duration, power, and spectral content—Only closed-loop contours that surround event maximum and are greater than the detection threshold were considered for property extraction. The contour at the lowest power level was selected as the event boundary contour 'B'. The region of the TF map within this boundary was defined as the ripple event, from which the relevant properties were extracted. Four properties were extracted from the event region. The first two were the times of event onset and offset for determination of the event duration. These onset and offset times were defined as the minimum and maximum time coordinates associated with the vertices of the boundary contour. The power of the HFO was then determined by calculating the mean power across all coordinate points of the TF map within the boundary B. Finally, the amplitude-weighted mean frequency of the HFO event was calculated using:

$$\overline{f_{hfo}} = \sum_i^B \frac{f_i * P_i}{\sum P_i} \quad (1)$$

where f_i and P_i and are the frequency and power amplitude of coordinate of the TF map within the boundary contour, B.

2.4.3. Illustrating detector methodology using simulated data—We used Gaussian functions of varying duration to simulate inter-ictal epileptiform spikes in computer generated 1 s data segments with a 2 kHz sampling rate. The Gaussians were generated using the function gausswin.m with $\sigma = 2, 3.3, 6.7$. We generated simulated ripples using a sine wave function with a frequency of 140 Hz and an amplitude of 350 μV, to correspond with the respective amplitude of the Gaussian function. A Blackman window was applied to the sine wave for the purpose of amplitude modulation. A simulated ripple on epileptiform spike was created by combining the Gaussian function ($\sigma = 6.7$) with the simulated ripple.

2.4.4. Quantifying detector performance using simulated data—A 1-s 2 kHz sampled iEEG trial was selected from one patient to calculate surrogate trials for the simulation study. This trial was selected on the basis of the absence of a ripple or inter-ictal epileptiform spike. We computed the fast-fourier transform of this iEEG trial (fft.m) for all frequencies less than the Nyquist frequency in 1 Hz bins. The imaginary components of the

FFT were permuted using randperm.m. iEEG surrogate trials were derived from the original iEEG trial using an inverse fast fourier transform (ifft.m) of the real and permuted imaginary components of the original iEEG trial. We then calculated the absolute value of the complex simulated signal. A simulated ripple with a frequency of 100 Hz and a duration of 0.0268 s was generated using a sine function enveloped by a Gaussian window of the form

$$e^{-\frac{1}{2}\left(\frac{2\alpha(n+\frac{N}{2}+1)}{N-1}\right)^2}$$ with $\alpha = 75$. The amplitude of the sine function ranged from from 2–30 µV in 2 µV steps to simulate varying ripple intensities. The simulated ripple was superimposed at 0.5 s on the 1000 permuted iEEG trials.

2.5. Validation of detector accuracy by visual inspection

The classification of ripple on spike events as true or false was validated using visual inspection of a custom display of the raw and processed patient data. In a single window each trial was displayed as (1) the unfiltered one second iEEG recording trial, (2) the iEEG trial following band-pass (80–240 Hz) filtering using a 500th order digital FIR filter, (3) vertical guidelines located at the peaks (green), and troughs (maroon) of the band-pass filtered signal superimposed on the unfiltered and filtered iEEG trial, (4) the TF plot, (5) the isopower contour lines resulting from the topographical analysis, (6) the candidate closed-loop contour group (green), or open-loop contour group (blue). True positive (TP) trials were defined as a true ripple on spike event confirmed by the detector and validated by visual inspection. False positive (FP) trials were defined as a true ripple on spike event confirmed by the detector, but no ripple on spike was evident on visual inspection. True negative (TN) trials were defined as a false ripple on spike event confirmed by the detector and validated by visual inspection. False negative (FN) trials were defined as a false ripple on spike event but visual inspection revealed a true ripple on spike event. Sensitivity was defined as TP/(TP + FN), Specificity as TN/(TN + FP), PPV as TP/(TP + FP), NPV as TN/(TN + FN), accuracy as (TP + TN)/(TP + FP+FN + TN). A second blinded visual inspection was performed in a similar manner with the exception that the TF plot, the isopower contour lines, and candidate groups were not displayed. The trials selected for this blinded visual inspection were a randomized group of an equal number of true and false ripple on spikes as defined by the un-blinded visual inspection.

The SOZ rate ratio for ripple events was calculated using

$$rr_{soz} = \left(\frac{Mean\ Event\ Rate_{SOZ} - Mean\ Event\ Rate_{NSOZ}}{Mean\ Event\ Rate_{SOZ} + Mean\ Event\ Rate_{NSOZ}}\right) \quad (2)$$

3. Results

3.1. Defining true and false high-frequency oscillations

To test the accuracy of the detector to discriminate true from false ripples on spikes (RonS), we used visual validation with the following criteria. A true RonS corresponded with a visible ripple superimposed on the spike in the unfiltered iEEG, and when the peaks and

troughs of the ripple riding the spike aligned with the peaks and troughs of the ripple evident after band-pass (80–240 Hz) filtering. In contrast, a false RonS was defined when a ripple was not evident on the spike in the unfiltered signal, or when the ripple that became evident after band-pass filtering, did not temporally align with the peaks and troughs in the unfiltered signal.

3.2. Illustration of detector principles

On the basis of these operational definitions, and assumptions we applied the detector to simulated data to illustrate how a topographical analysis of time frequency spectrograms could differentiate true and false ripples on spikes. The time frequency plots of Gaussians with durations of $\sigma > 1.0$ms were described by a set of OLCs of isopower extending up from the lower frequency limit (80 Hz), reaching a peak frequency inversely proportional to the duration of the Gaussian signal (Fig. $1A_{1,2}$). When the duration of the Gaussian was decreased to $\sigma \sim 1.0$ms, a group of CLCs of isopower were evident (Fig. $1A_3$). Since no true ripple oscillation was present during the Gaussians, the peaks and troughs of the band-pass filtered simulated signals showed incomplete correspondence with the raw simulated signal (Fig. $1A_{1-3}$).

A simulated ripple event resulted in a CLC group of isopower centered at the simulated ripple's mean frequency (Fig. $1B_1$, green region). In this case, the peaks and troughs of the band-pass filtered signal did coincide with the raw simulated signal (Fig. $1B_1$, top black and red waveform). When the simulated ripple event was combined with a Gaussian the detector registered a set of OLCs extending from the lower frequency limit and a CLCs group centered at the ripple's mean frequency (Fig. $1B_2$, green and maroon), and the peaks and troughs of the raw signal corresponded with the peaks and troughs of the band-pass filtered signal (Fig. $1B_2$, top black and red waveform).

3.3. Measuring detector performance using simulated data

Using simulated iEEG data, we sought to determine the stability and variability of ripple identification and characterization. Ripples of a predetermined magnitude, identical in duration and spectral content, were superimposed on simulated iEEG trials.

Since the topographical algorithm is designed to identify a closed or open loop contour group, regardless of the power of the group, we first asked what fraction of the simulated iEEG trials, lacking a superimposed simulated ripple, would result in a closed loop contour. We found that when no ripple was present in the simulated data, the detector identified closed loop groups in 41.5% of the trials (Fig. 2A). The mean average power magnitude detected for these false positive events corresponded to ripple amplitudes <5 μV (Fig. 2B).

We next introduced the superimposed ripple to the simulated iEEG background. We found that the probability of false negative ripple identification decreased exponentially with increased simulated ripple amplitude. As the simulated ripple amplitude was increased, the average power weighted mean frequency estimated by the detector approached a frequency of 101.6 Hz, slightly above the frequency of the simulated ripple of 100 Hz. The standard deviation of the average frequency of the detected ripple decreased exponentially (Fig. 2C).

Increasing the amplitude of the simulated ripple corresponded with an increase in the power of the identified ripple, as well as an increase in the standard deviation of this measurement (Fig. 2B). Finally, the increasing amplitude also corresponded with a decrease in the variability of the detected ripple duration. The simulated ripple duration was consistently underestimated by the topographical method (Fig. 2D).

3.4. iEEG visual verification and detector performance

The detector was applied to 25,011 one-second iEEG trials, recorded from 12 patients undergoing intracranial monitoring with depth electrodes (Table 1), that recorded RonS events. In all these trials the detector could differentiate the true RonS trials from the false RonS trials, and characterize the properties of the former. False RonS have no mean spectral content, or centroid of power since they result from filter ringing. We randomly selected 2934 trials for visual verification. A true positive was defined as a trial in which the detector identified a CLC group, a true RonS event was clear in the raw signal, and, as we assumed (see 3.1), the peaks and troughs of the raw signal corresponded with those of the band-pass filtered signal (Fig. 3A1,2). A false positive was defined as an instance in which the detector identified a CLC group, but a true RonS event was not clear in the raw signal. True negative cases corresponded to sharply contoured inter-ictal discharges without ripples i.e. false RonS (Fig. 3B1,2). A true negative was defined as an instance in which the detector identified only sets of OLCs, a ripple was not evident in the raw signal. A false negative was defined as a case in which the detector only identified sets of OLCs when a true RonS was evident in the raw iEEG signal, or alternatively if the trial failed to exhibit an epileptiform discharge.

Table 2 provides a summary of the detector's performance for distinguishing true from false ripples on spikes across the 12 patients when the time-frequency was provided to the reviewer (i.e. un-blinded). Across all patients, the detectors accuracy was $88.5 \pm 2.1\%$, with a sensitivity of $81.8 \pm 3.4\%$, a specificity of $95.2 \pm 0.81\%$, a precision of $94.5 \pm 1.8\%$, and a negative predictive value of $84.0 \pm 3.9\%$ (s.e.m, n = 12). For all the patients, a second reviewer visually validated the detector performance with a Cohen's kappa equal to 0.37, kappa values for individual patients ranged between 0.11–0.61.

Table 3 provides a summary of the detector's performance for distinguishing true from false ripples on spikes across the 12 patients when the reviewer was blinded to the time-frequency map. Across all patients, and two expert reviewers (ZW, SAW), the detectors accuracy was $68.0 \pm 2.0\%$, with a sensitivity of $74.46 \pm 3.14\%$, a specificity of $61.30 \pm 2.94\%$, a precision of $66.23 \pm 1.97\%$, and a negative predictive value of $72.10 \pm 2.56\%$. The Cohen's kappa across the two reviewers was equal to 0.01, kappa values for individual patients ranged between −0.14–0.25.

3.5. Properties of detected ripples

We examined the properties of the true RonS events that were identified by the detector and visually verified (Table 4). For each detected RonS event, the mean power, power-weighted mean frequency, and event duration were quantified. For the combined verified trials, the true RonSs had a mean frequency of 109.4 ± 24.7Hz. The detector had the capability of distinguishing fast ripples from ripples, an example of which can be seen in Fig. 4. The true

RonS had a mean power magnitude of $47.9 \pm 175.6 * 10^5$ *arbitrary units*, and a mean duration of 20.5 ± 12.8ms True RonS power magnitude was inconsistent across individual trials, electrodes, and patients (Table 3). Mean event duration was also variable, but the mean duration corresponded to only two cycles of the mean RonS oscillation period. We also quantified the SOZ rate ratio for all the true and false RonS events identified in the study (Table 4).

3.6. Detector confounds

For true RonS detections an underestimation of accurate event duration manifested in two distinct contexts; first, in some trials, a large CLC group representing a ripple event was separated into smaller component CLC groups (Fig. 5A$_1$). Second, correct ripple events with a spectral content near the lower limit (80 Hz) of the time-frequency plot had fewer CLCs, and consequently a shorter duration (Fig. 5A$_2$). Overall $30.2 \pm 14.4\%$ of true RonS detections were erroneously brief.

False RonS detections were sometimes true RonS events with a superimposed burst (30–400 ms) of gamma (30–80 Hz) oscillations that produced OLCs (Fig. 6A). In these cases, the detector could not differentiate between OLCs produced by the gamma oscillations, and the OLCs that would result from filter ringing. Consequently, false RonS detections could also result from gamma events even in the absence of a superimposed ripple (Fig. 6B). Overall $7.31 \pm 6.09\%$ of the RonS trials were contaminated by gamma event detections.

4. Discussion

This study presents an automated analysis of iEEG recordings based on defining the topographic features of time-frequency plots using isopower contours. The topographical method requires that HFO events are first detected in continuous iEEG recordings, by a separate and distinct process, prior to ripple identification, classification, and characterization. Following ripple detection, the topographical method was capable of successfully differentiating the true ripple on spike (RonS) events from false RonS, as well as quantifying the RonS properties such as spectral content, power, and duration. The success of our algorithm helps to validate the central premise that "blobs" of power in time-frequency spectrograms are representative of distinct ripple oscillations, while "candles" are representative of sharply contoured epileptiform discharges.

4.1. Utility of the detector

There is strong evidence that HFOs are a biomarker of epileptogenic brain (Jacobs et al., 2008), and utilizing HFO rates for clinical applications will require accurate HFO detection (Cimbalnik et al., 2016), and an agreed upon ripple classification scheme. Quantifying HFO rates using iEEG recordings from the epilepsy monitoring unit or operating room has been proposed as a means to identify epileptogenic brain regions (van 't Klooster et al., 2015a, 2015b) and studies have suggested that simultaneous HFOs and inter-ictal epileptiform spikes (IES) are stronger indicators of epileptogenic tissue than IES events alone (Jacobs et al., 2008). A major challenge in the accurate evaluation of these biomarkers is that artifacts and sharp IESs can mimic HFOs when filtered. The method presented in this study has the

advantage of being able to identify true HFOs while excluding and demarcating false HFOs due to sharp transients. In the un-blinded visual verification of the detector performance it is likely that the measured accuracy of our detector for distinguishing true and false ripples is inflated, since the gold standard (*i.e.* visual inspection) was not external or independent of the experimental procedure being validated. In the blinded visual verification of the detector performance in which the time-frequency maps were not displayed to the reviewers, the accuracy of the detector was only 68.0%. Another published algorithm to distinguish true from false ripples on spikes reported an accuracy of 76.6% on the basis of a similar blinded review (Amiri et al., 2016). However, inter-rater agreement was very poor in our blinded visual verification, suggesting that it is challenging to differentiate true from false ripples on spikes on the basis of visual inspection alone. For example, very small amplitude true ripple on spike events can be difficult to distinguish on the basis of visual inspection.

Though it remains uncertain that true HFOs exhibit superior accuracy for delineating epileptogenic brain regions, as compared with sharply contoured IES events (Burnos et al., 2016), the subject merits further investigation. Furthermore, only true ripple on spike events can be assigned properties such as mean spectral content, power, and duration.

4.2. Methodological aspects

A contour analysis of the time-frequency plot resulting from a wavelet convolution could be successfully used to distinguish true from false RonS because the brain signals do not exhibit discontinuities and therefore its discrete time-frequency map represents a continuous surface. The approach of using contour analysis to define high-frequency oscillations has the distinct advantage of being able to identify multiple events that overlap in time but are distinct in spectral content, even when superimposed on a sharp transient.

Although the detector succeeded to distinguish true from false RonS events in the vast majority of the trials, several limitations of this method were evident.

First, the illustrative simulation results demonstrated that very brief, and sharply contoured, transient events are falsely detected as a true RonS. This pitfall is due to an inverse relationship between the frequency of the peak power magnitude and the duration of the Gaussian transient. While in inter-ictal iEEG recordings, inter-ictal epileptiform spike (IES) events are generally not of sufficient brevity to produce this confound for our detector, ictal data may exhibit such events. Potentially, this artifact could be reduced with the selection of more appropriate mother wavelets or recording at higher sampling rates.

It is also theoretically plausible that the 'candle' produced in the time-frequency plot by a sharp transient event may overlap with the blob produced by a simultaneously occurring true ripple. This overlap could render the topographical analysis ineffective. Visual validation of the methodology indicates that this was a rare occurrence in these iEEG recordings, however it could account for a subset of the false negative results.

One serious shortcoming of the detector was the frequent underestimation of the duration of true RonS events. This occurred because the CLC groups associated with the detected RonS were often surrounded by OLCs due to the simultaneous IES. Also, very low frequency

ripples exhibited some OLC because of the minimum frequency of 50 Hz interest chosen for the topographical analysis. It is likely that repeating the topographical analysis in a lower frequency range for ripples of a relatively lower spectral content can result in an improvement in the estimation of event duration. Alternatively, duration was underestimated when a single ripple was detected as several distinct CLC groups, rather than a single consolidated group. This error could potentially be overcome by increasing the number of generated contours, using recordings with higher sampling rates, or introducing alternative strategies for identifying or rejecting CLC groups. A further possibility is increasing the Gaussian width of the Morlet wavelet within certain frequency ranges.

Lastly, rare bursts of gamma activity, distinct from IES events, could generate OLC groups and generate false negative results. This confound could potentially be corrected by separately inspecting the topography of the time-frequency plot in the beta and gamma band to distinguish between "candles" representing inter-ictal epileptiform spikes and "blobs" of power representing gamma activity.

4.3. Conclusion and future directions

This study presents a new method for distinguishing true RonS events from the false RonS events that result from filter ringing. This method is based on the analysis of isopower contours generated by topographically analyzing the time-frequency plot. Utilization of this method will assist in the determination of whether true HFO events are generated by distinct mechanisms as compared with false HFO events. Further, it will aid in the investigation of true and false RonS with respect to understanding and differentiating their mechanisms of generation (Schevon et al., 2009; Keller et al., 2010), utility for identifying epileptogenic regions (Burnos et al., 2016), role during seizures (Eissa et al., 2016), and also their ability to disrupt normal cognition (Horak et al., 2017). The topographical method we describe is one of many "computer vision" based approaches to identifying multiple distinct brief oscillatory events that overlap in time, but are unique in spectral content (Burnos et al., 2014; Kucewicz et al., 2017). One remaining concern is whether time-frequency analysis on 1-s EEG epochs is reliable. The reliability of the measurements of ripple properties including power, spectral content, and duration can likely be improved by pre-whitening or normalizing the data (Roehri et al., 2016). This technique should be generalizable to both scalp (Andrade-Valenca et al., 2011) and other types of intracranial electrical recordings, and could also be extended to identify and characterize fast-ripple oscillations.

Acknowledgments

References

Amiri M, Lina JM, Pizzo F, Gotman J. High frequency oscillations and spikes: separating real HFOs from false oscillations. Clin Neurophysiol. 2016; 127:187–96. [PubMed: 26100149]

Andrade-Valenca LP, Dubeau F, Mari F, Zelmann R, Gotman J. Interictal scalp fast oscillations as a marker of the seizure onset zone. Neurology. 2011; 77:524–31. [PubMed: 21753167]

Bell AJ, Sejnowski TJ. The "independent components" of natural scenes are edge filters. Vision Res. 1997; 37:3327–38. [PubMed: 9425547]

Bénar CG, Chauvière L, Bartolomei F, Wendling F. Pitfalls of high-pass filtering for detecting epileptic oscillations: a technical note on "false" ripples. Clin Neurophysiol. 2010; 121:301–10. [PubMed: 19955019]

Birot G, Kachenoura A, Albera L, Bénar C, Wendling F. Automatic detection of fast ripples. J Neurosci Methods. 2013; 213:236–49. [PubMed: 23261773]

Bragin A, Wilson CL, Staba RJ, Reddick M, Fried I, Engel J Jr. Interictal high-frequency oscillations (80–500 Hz) in the human epileptic brain: entorhinal cortex. Ann Neurol. 2002; 52:407–15. [PubMed: 12325068]

Burnos S, Hilfiker P, Sürücü O, Scholkmann F, Krayenbühl N, Grunwald T, Sarnthein J. Human intracranial high frequency oscillations (HFOs) detected by automatic time-frequency analysis. PLoS One. 2014; 9:e94381. [PubMed: 24722663]

Burnos S, Frauscher B, Zelmann R, Haegelen C, Sarnthein J, Gotman J. The morphology of high frequency oscillations (HFO) does not improve delineating the epileptogenic zone. Clin Neurophysiol. 2016; 127:2140–8. [PubMed: 26838666]

Cimbalnik J, Kucewicz MT, Worrell G. Interictal high-frequency oscillations in focal human epilepsy. Curr Opin Neurol. 2016; 29:175–81. [PubMed: 26953850]

Csicsvari J, Hirase H, Czurkó A, Mamiya A, Buzsáki G. Fast network oscillations in the hippocampal CA1 region of the behaving rat. J Neurosci. 1999; 19(16):RC20. [PubMed: 10436076]

Dvorak D, Fenton AA. Toward a proper estimation of phase-amplitude coupling in neural oscillations. J Neurosci Methods. 2014; 225:42–56. [PubMed: 24447842]

Eissa TL, Tryba AK, Marcuccilli CJ, Ben-Mabrouk F, Smith EH, Lew SM, et al. Multiscale Aspects of Generation of High-Gamma Activity during Seizures in Human Neocortex. eNeuro. 2016; 3(2) pii.

Engel J Jr, Bragin A, Staba R, Mody I. High-frequency oscillations: what is normal and what is not? Epilepsia. 2009; 50:598–604. [PubMed: 19055491]

Engel J Jr, McDermott MP, Wiebe S, Langfitt JT, Stern JM, Dewar S, Sperling MR, Gardiner I, Erba G, Fried I, Jacobs M, Vinters HV, Mintzer S, Kieburtz K. Early Randomized Surgical Epilepsy Trial (ERSET) Study Group. Early surgical therapy for drug-resistant temporal lobe epilepsy: a randomized trial. JAMA. 2012; 307:922–30. [PubMed: 22396514]

Gardner AB, Worrell GA, Marsh E, Dlugos D, Litt B. Human and automated detection of high-frequency oscillations in clinical intracranial EEG recordings. Clin Neurophysiol. 2007; 118:1134–43. [PubMed: 17382583]

Gotman J. High frequency oscillations: the new EEG frontier? Epilepsia. 2010; 51:63–5. [PubMed: 20331719]

Horak PC, Meisenhelter S, Song Y, Testorf ME, Kahana MJ, Viles WD, Bujarski KA, Connolly AC, Robbins AA, Sperling MR, Sharan AD, Worrell GA, Miller LR, Gross RE, Davis KA, Roberts DW, Lega B, Sheth SA, Zaghloul KA, Stein JM, Das SR, Rizzuto DS, Jobst BC. Interictal epileptiform discharges impair word recall in multiple brain areas. Epilepsia. 2017; 58:373–80. [PubMed: 27935031]

Jacobs J, LeVan P, Chander R, Hall J, Dubeau F, Gotman J. Interictal high-frequency oscillations (80–500 Hz) are an indicator of seizure onset areas independent of spikes in the human epileptic brain. Epilepsia. 2008; 49:1893–907. [PubMed: 18479382]

Jacobs J, Staba R, Asano E, Otsubo H, Wu JY, Zijlmans M, Mohamed I, Kahane P, Dubeau F, Navarro V, Gotman J. High-frequency oscillations (HFOs) in clinical epilepsy. Prog Neurobiol. 2012; 98:302–15. [PubMed: 22480752]

Keller CJ, Truccolo W, Gale JT, Eskandar E, Thesen T, Carlson C, Devinsky O, Kuzniecky R, Doyle WK, Madsen JR, Schomer DL, Mehta AD, Brown EN, Hochberg LR, Ulbert I, Halgren E, Cash SS. Heterogeneous neuronal firing patterns during interictal epileptiform discharges in the human cortex. Brain. 2010; 133:1668–81. [PubMed: 20511283]

Kucewicz MT, Berry BM, Kremen V, Brinkmann BH, Sperling MR, Jobst BC, Gross RE, Lega B, Sheth SA, Stein JM, Das SR, Gorniak R, Stead SM, Rizzuto DS, Kahana MJ, Worrell GA.

Dissecting gamma frequency activity during human memory processing. Brain. 2017; 140:1337–50. [PubMed: 28335018]

Liu S, Sha Z, Sencer A, Aydoseli A, Bebek N, Abosch A, Henry T, Gurses C, Ince NF. Exploring the time-frequency content of high frequency oscillations for automated identification of seizure onset zone in epilepsy. J Neural Eng. 2016; 13:026026. [PubMed: 26924828]

Roehri N, Lina JM, Mosher JC, Bartolomei F, Benar CG. Time-Frequency Strategies for Increasing High-Frequency Oscillation Detectability in Intracerebral EEG. IEEE Trans Biomed Eng. 2016; 63:2595–606. [PubMed: 27875125]

Schevon CA, Trevelyan AJ, Schroeder CE, Goodman RR, McKhann G Jr, Emerson RG. Spatial characterization of interictal high frequency oscillations in epileptic neocortex. Brain. 2009; 132:3047–59. [PubMed: 19745024]

Shimamoto S, Waldman Z, Orosz I, Song I, Bragin A, Fried I, Engel J Jr, Staba R, Sharan A, Wu C, Sperling MR, Weiss SA. Utilization of independent component analysis for accurate pathological ripple detection in intracranial EEG recordings recorded extra- and intra-operatively. Clin Neurophysiol. 2018; 129(1):296–307. [PubMed: 29113719]

Staba RJ, Wilson CL, Bragin A, Fried I, Engel J Jr. Quantitative analysis of highfrequency oscillations (80–500 Hz) recorded in human epileptic hippocampus and entorhinal cortex. J Neurophysiol. 2002; 88:1743–52. [PubMed: 12364503]

van 't Klooster MA, Leijten FS, Huiskamp G, Ronner HE, Baayen JC, van Rijen PC, Eijkemans MJ, Braun KP. Zijlmans MHFO study group. High frequency oscillations in the intra-operative ECoG to guide epilepsy surgery ("The HFO Trial"): study protocol for a randomized controlled trial. Trials. 2015a; 16:422. [PubMed: 26399310]

van 't Klooster MA, van Klink NE, Leijten FS, Zelmann R, Gebbink TA, Gosselaar PH, Braun KP, Huiskamp GJ, Zijlmans M. Residual fast ripples in the intraoperative corticogram predict epilepsy surgery outcome. Neurology. 2015b; 85:120–8. [PubMed: 26070338]

Weiss SA, Alvarado-Rojas C, Bragin A, Behnke E, Fields T, Fried I, Engel J Jr, Staba R. Ictal onset patterns of local field potentials, high frequency oscillations, and unit activity in human mesial temporal lobe epilepsy. Epilepsia. 2016a; 57:111–21. [PubMed: 26611159]

Weiss SA, Orosz I, Salamon N, Moy S, Wei L, Van't Klooster MA, Knight RT, Harper RM, Bragin A, Fried I, Engel J Jr, Staba RJ. Ripples on spikes show increased phase-amplitude coupling in mesial temporal lobe epilepsy seizure-onset zones. Epilepsia. 2016b; 57:1916–30. [PubMed: 27723936]

Wiebe S, Blume WT, Girvin JP, Eliasziw M. Effectiveness and Efficiency of Surgery for Temporal Lobe Epilepsy Study Group. A randomized, controlled trial of surgery for temporal-lobe epilepsy. N Engl J Med. 2001; 345:311–8. [PubMed: 11484687]

Zelmann R, Zijlmans M, Jacobs J, Châtillon CE, Gotman J. Improving the identification of High Frequency Oscillations. Clin Neurophysiol. 2009; 120:1457–64. [PubMed: 19576848]

Zelmann R, Mari F, Jacobs J, Zijlmans M, Dubeau F, Gotman J. A comparison between detectors of high frequency oscillations. Clin Neurophysiol. 2012; 123:106–16. [PubMed: 21763191]

HIGHLIGHTS

- A topographical analysis of time-frequency plots can characterize ripple properties.

- This same analysis can classify true ripple on epileptiform spike events from filter ringing.

- The rates of true ripple on spike events and very sharply contoured spikes are elevated in epileptogenic regions.
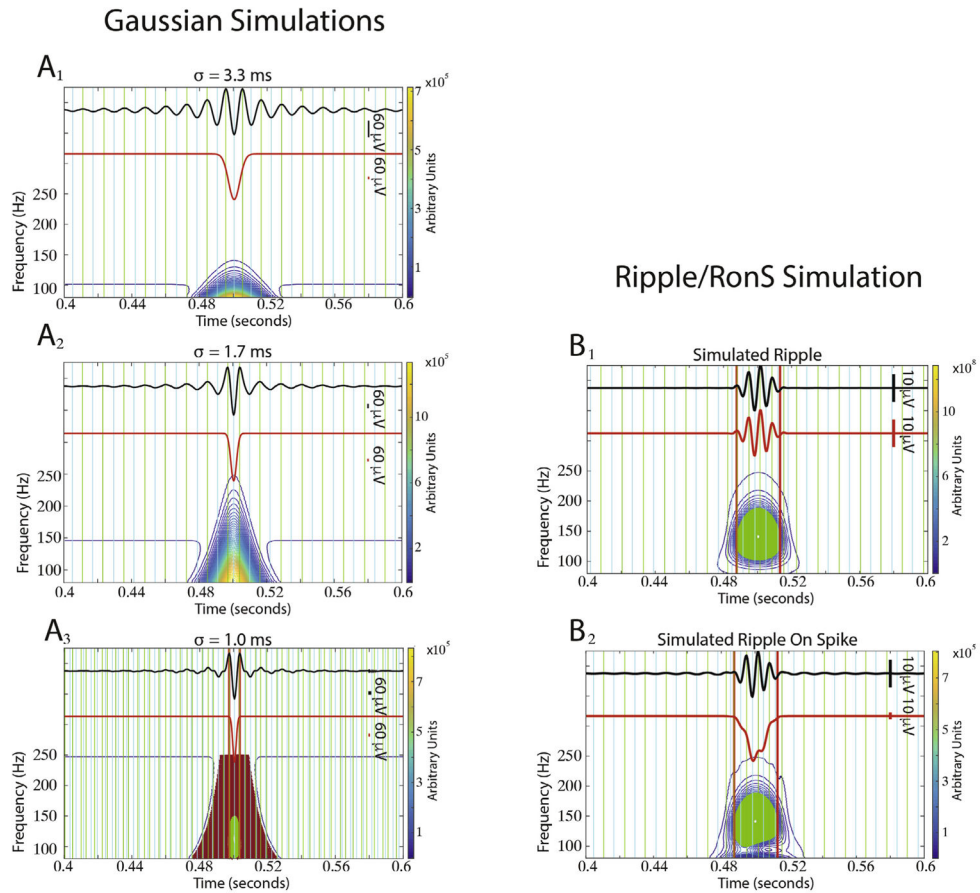
Gaussian Simulations

Ripple/RonS Simulation

Fig. 1.
Illustration of detector principles using simulated data. Topographical analysis of the time-frequency plot of wavelet convolution of Gaussian waveforms results in open loop contours (A_1, A_2), or closed loop contours (A_3) depending on the standard deviation of the Gaussian waveform. A simulated ripple without a Gaussian (B_1) results in closed loop contours and no open loop contours. When the simulated ripple is combined with a Gaussian both open- and closed loop contours are evident representing both events (B_2). Green and blue vertical line are positive and negative peaks in the band-pass filtered signal, respectively. (For interpretation of the references to colour in this figure legend, the reader is referred to the web version of this article.)
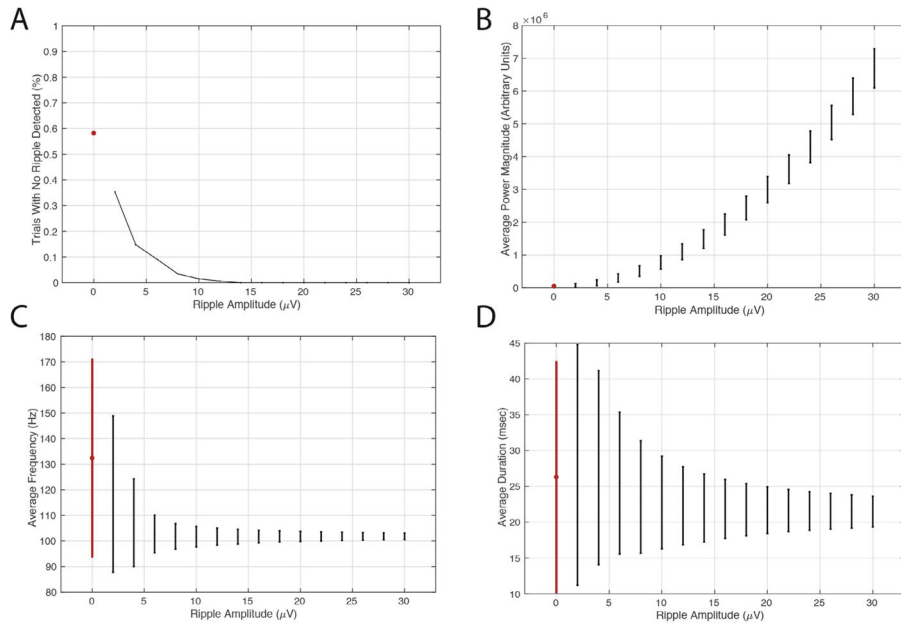
Fig. 2.
Measuring detector performance using simulated data. (A) The percentage of false negative ripple detections identified in the surrogate iEEG data trials as a function of the amplitude of the simulated ripple. (B) Detected simulated ripple power. (C) Detected simulated ripple duration. (D) Detected simulated ripple power weighted mean frequency. Error bars show standard deviation.

True Ripple on Spike Detections

False Ripple on Spike Detections
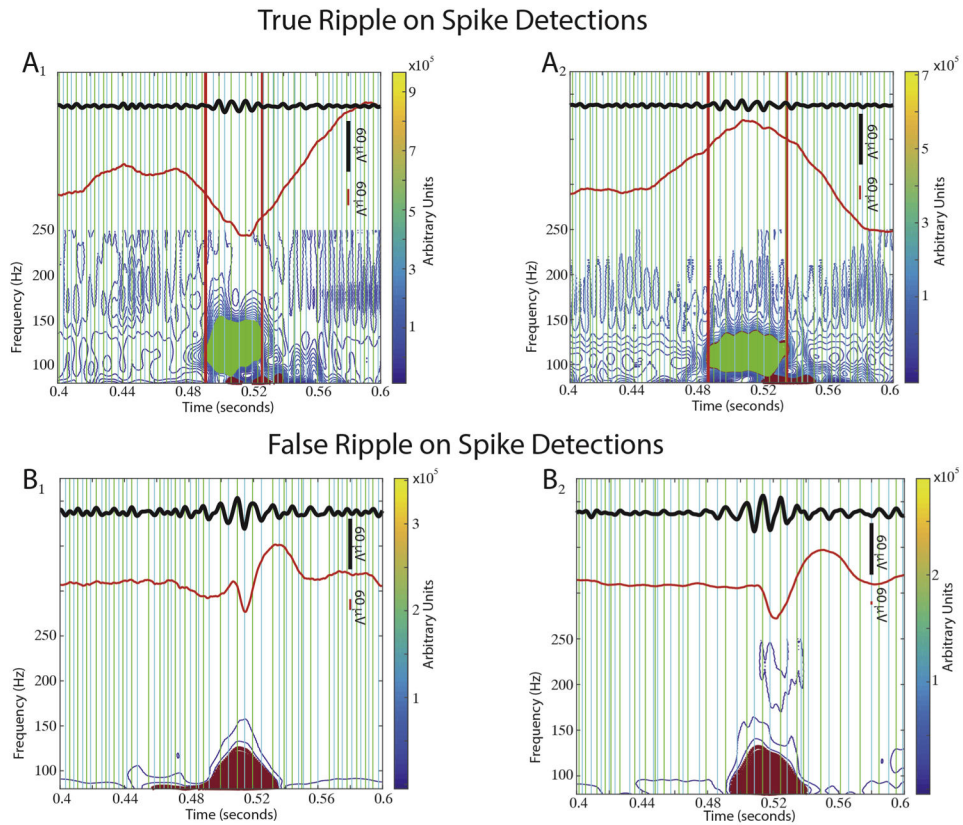
Fig. 3.

Detector performance with human intracranial electroencephalogram (iEEG) recordings. (A) Two examples of true ripples on spikes, and (B) two examples of false ripples on spikes correctly classified by the detector. The 80–240 Hz band-pass filtered iEEG waveforms, (Middle, red) unfiltered iEEG waveform, (bottom) time-frequency representation of the iEEG waveform following contour processing, and closed loop detection algorithms, with the group of closed loop contours representing the ripple shown in green, and the group of open loop contours representing the spike shown in magenta. Green and blue vertical line are positive and negative peaks in the band-pass filtered signal, respectively. Vertical red lines indicate the beginning and end times of the characterized ripple event. (For interpretation of the references to colour in this figure legend, the reader is referred to the web version of this article.)

Differentiating Ripples From Fast Ripples on Spikes

Fig. 4.
The detector can correctly differentiate ripple from fast ripple events that occur of epileptiform discharges. The 80–240 Hz band-pass filtered iEEG waveforms, (Middle, red) unfiltered iEEG waveform, (bottom) time-frequency representation of the iEEG waveform following contour processing, and closed loop detection algorithms, with the group of closed loop contours representing the ripple shown in green, and the group of closed loop contours representing the fast ripple shown in magenta. Green and blue vertical line are positive and negative peaks in the band-pass filtered signal, respectively. Vertical red lines indicate the beginning and end times of the characterized ripple event. (For interpretation of the references to colour in this figure legend, the reader is referred to the web version of this article.)
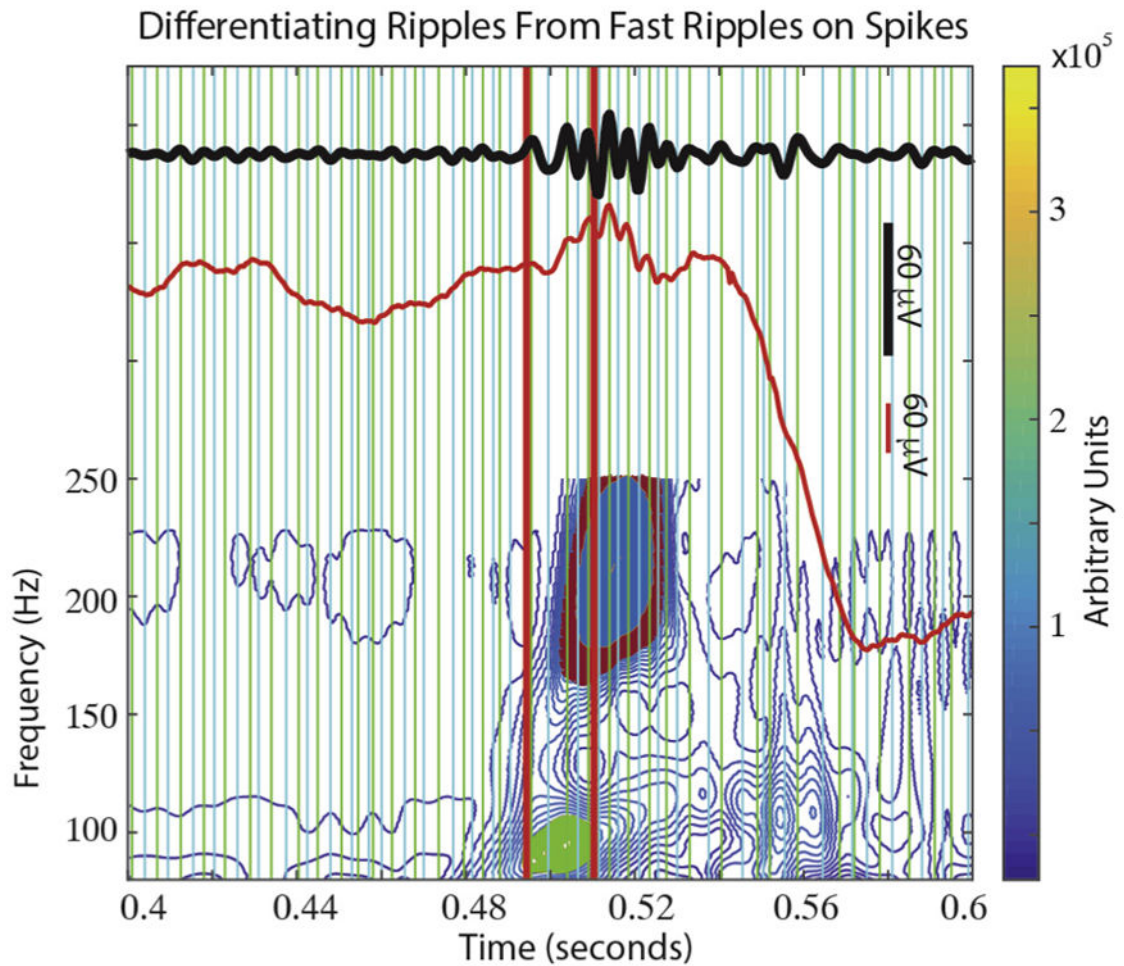
Brief Detection Events
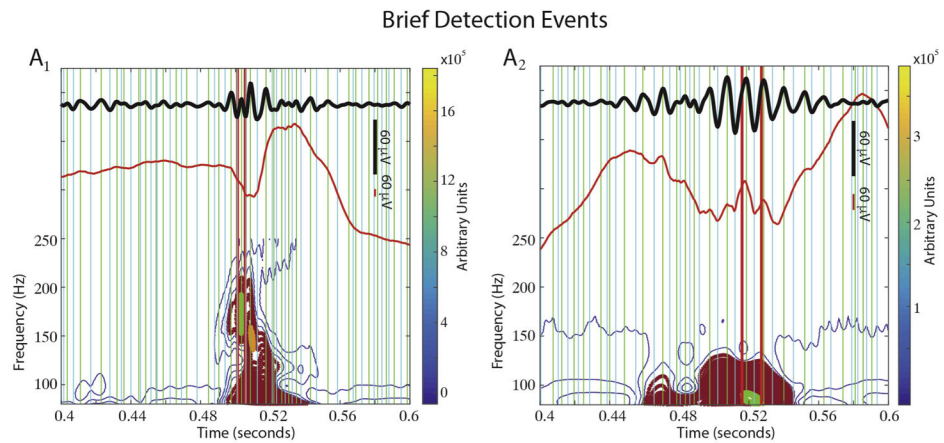
Fig. 5.
True ripple on spike event characterization was confounded by the identification of brief events, that underestimated ripple event duration and power. The 80–240 Hz band-pass filtered iEEG waveforms, (Middle, red) unfiltered iEEG waveform, (bottom) time-frequency representation of the iEEG waveform following contour processing, and closed loop detection algorithms, with the group of closed loop contours representing the ripple shown in green, and the group of open loop contours representing the spike shown in magenta, and a group of contours in orange as a second ripple event (A_1). Green and blue vertical line are positive and negative peaks in the band-pass filtered signal, respectively. Vertical red lines indicate the beginning and end times of the characterized ripple event. (For interpretation of the references to colour in this figure legend, the reader is referred to the web version of this article.)

Gamma Detection Events
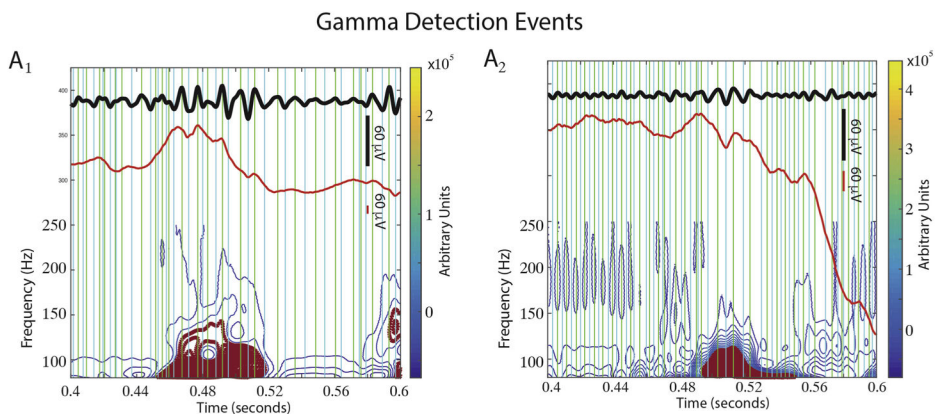
Fig. 6.
False ripple on spike detection was confounded by gamma oscillation events that produced open contours and mimicked sharp transients. The 80–240 Hz band-pass filtered iEEG waveforms, (Middle, red) unfiltered iEEG waveform, (bottom) time-frequency representation of the iEEG waveform following contour processing, and closed loop detection algorithms, the group of open loop contours representing the gamma activity is shown in magenta. Green and blue vertical line are positive and negative peaks in the band-pass filtered signal, respectively. (For interpretation of the references to colour in this figure legend, the reader is referred to the web version of this article.)

Table 1

Patient characteristics. iEEG: intracranial EEG, IED: inter-ictal epileptiform discharge, SOZ: seizure-onset zone, N/A: not applicable i.e. no resection, FCD: focal cortical dysplasia.

Patient Age Sex	Duration of epilepsy	Risk Factors	Scalp EEG	MRI	PET hypometabolic	iEEG IED	iEEG SOZ	Pathology
448, 52, M	16 yrs	Stroke	Left temporal	Left PCA infarct	Left temporal hypometabolism	Left mesial and neocortical temporal	Left mesial temporal	gliosis
449. 36, M	24 yrs	Stroke	None	None localizable	Left perisylvian encephalomalacia	Left parietal-occipital	Left parietal-occipital	gliosis
451, 52, F	22 yrs	NF1	Left and right temporal	Right inferior gyrus T2 signal	Left temporal hypometabolism	Left and right mesial temporal	Left and right mesial temporal	N/A
453, 41, F	14 yrs	None	Left and right temporal	T2 signal in left and right temporal pole and mesial temporal structures	Right temporal hypometabolism	Left and right mesial temporal	Right temporal	FCD
454, 45, M	34 yrs	Meningitis	Left temporal	T2 signal in left lateral temporal lobe	Left frontal, insular, and temporal lobe	Left frontal, insular, and temporal	Left frontal, insular, and temporal	N/A
456, 35, F	12 yrs	None	Right temporal	Normal s/p RNS removal	Right temporal	Right mesial temporal	Right mesial and lateral temporal	gliosis
463, 27, M	10 yrs	None	Left and right temporal	Right hippocampal sclerosis, prior right AVM resection.	Hypometabolism around prior AVM resection.	Right and left temporal	Right and left temporal.	none
467, 23, F	16 yrs	None	Left centro-parietal	Left parietal focal cortical dysplasia	Left parietal and occipital	Left parietal	Left parietal	FCDIIb
470, 49, F	30 yrs	None	Left temporal	Left hippocampal sclerosis	Left temporal	Left temporal	Left temporal	none
472,43, F	27 yrs	Febrile seizures	Left and right temporal	R. temporal craniotomy and hippocampal resection	Right temporal	Left mesial temporal, right orbitofrontal	Left mesial temporal, right orbitofrontal	N/A
473, 69, M	5 yrs	TBI	Left and right temporal	Left hippocampal sclerosis	Left temporal and orbitofrontal hypometabolism	Left and right temporal	Left temporal	None
474, 43, F	6 yrs	TBI	Left and right temporal	Microbleed in right centrum ovale	Right temporal hypometabolism	Left and right temporal	Left and right temporal	None

Table 2

True and false ripple on spike detector sensitivity, specificity, precision i.e. positive predictive value (PPV), and negative predictive value (NPV) for differentiating the two event types in the 12 study patient in an un-blinded review.

Patient ID	Accuracy	Sensitivity	Specificity	Precision (PPV)	NPV
448 ($n = 206$)	0.84	0.68	0.91	0.76	0.87
449 ($n = 128$)	0.93	0.92	0.97	0.99	0.76
451 ($n = 400$)	0.91	0.92	0.9	0.91	0.91
453 ($n = 200$)	0.73	0.55	0.96	0.94	0.63
454 ($n = 400$)	0.95	0.93	0.96	0.93	0.96
456 ($n = 400$)	0.81	0.76	0.96	0.98	0.58
463 ($n = 463$)	0.84	0.79	0.94	0.96	0.67
467 ($n = 200$)	0.95	0.92	0.97	0.94	0.95
470 ($n = 200$)	0.92	0.8	0.98	0.97	0.89
472 ($n = 200$)	0.98	0.91	1	1	0.97
473 ($n = 200$)	0.91	0.84	0.96	0.95	0.89
474 ($n = 200$)	0.85	0.78	0.94	0.94	0.78
All Patients ($n = 2934$)	0.89	0.82	0.95	0.94	0.84

Table 3

True and false ripple on spike detector sensitivity, specificity, precision i.e. positive predictive value (PPV), and negative predictive value (NPV) for differentiating the two event types in the 12 study patients in a blinded review by two experts conducted without spectrogram display.

Patient ID	Accuracy	Sensitivity	Specificity	Precision (PPV)	nPV	Kappa	K. err
448 (n = 50)	0.78/0.72	0.72/0.75	0.84/0.64	0.82/0.69	0.75/0.76	−0.14	0.14
449 (n = 62)	0.71/0.58	0.97/0.52	0.45/0.65	0.64/0.59	0.94/0.57	0.03	0.12
451 (n = 272)	0.82/0.66	0.89/0.94	0.74/0.38	0.78/0.6	0.87/0.87	0.07	0.07
453 (n = 86)	0.71/0.57	0.84/0.74	0.58/0.4	0.67/0.55	0.78/0.61	−0.12	0.12
454 (n = 210)	0.74/0.74	0.71/0.85	0.76/0.63	0.75/0.70	0.73/0.81	0.08	0.07
456 (n = 192)	0.71/0.65	0.82/0.79	0.60/0.50	0.68/0.61	0.77/0.71	−0.10	0.08
463 (n = 116)	0.57/0.62	0.60/0.66	0.53/0.59	0.57/0.61	0.57/0.63	−0.12	0.09
467 (n = 108)	0.80/0.71	0.78/0.70	0.82/0.72	0.81/0.72	0.79/0.71	0.07	0.10
470 (n = 72)	0.61/0.63	0.67/0.81	0.56/0.44	0.60/0.59	0.63/0.70	−0.04	0.12
472 (n = 36)	0.56/0.50	0.50/0.44	0.61/0.56	0.56/0.50	0.55/0.50	−0.08	0.17
473 (n = 72)	0.71/0.67	0.58/0.75	0.83/0.58	0.78/0.64	0.67/0.70	0.25	0.11
474 (n = 94)	0.82/0.72	0.89/0.89	0.89/0.55	0.78/0.67	0.88/0.84	0.02	0.11
All Patients (n = 1370)	0.73/0.66	0.75/0.74	0.67/0.55	0.70/0.62	0.74/0.70	0.01	0.03

Table 4

Properties of detected ripple on spike events for verified trials. The mean and standard deviation of the average power magnitude, weighted mean frequency, duration of detected true ripple on spike events from the verified trials of each patient individually and combined. The TRonS and FRonS SOZ rate ratio for all the analyzed trials is also shown.

Patient	Mean Power (10^5 arbitrary units)	Mean Frequency (Hz)	Mean Duration (ms)	TRonS SOZ rate ratio	FRonS SOZ rate ratio
448 ($n = 206$)	6.69 ± 9.12	104.95 ± 22.02	15.43 ± 10.52	0.922	0.963
449 ($n = 128$)	14.66 ± 13.86	111.65 ± 21.85	24.11 ± 13.06	0.667	0.77
451 ($n = 400$)	29.90 ± 141.06	108.00 ± 19.76	21.64 ± 13.60	0.649	0.861
453 ($n = 200$)	33.55 ± 46.12	109.48 ± 25.67	17.98 ± 10.24	0.29	0.546
454 ($n = 400$)	98.46 ± 224.80	122.66 ± 29.17	23.11 ± 13.42	0.665	0.623
456 ($n = 400$)	42.98 ± 65.80	102.90 ± 19.20	22.72 ± 13.70	0.703	0.7
463 ($n = 463$)	18.35 ± 15.50	118.86 ± 33.85	25.41 ± 12.92	0.832	0.941
467 ($n = 200$)	30.84 ± 38.26	104.74 ± 18.51	18.28 ± 10.47	0.711	0.868
470 ($n = 200$)	94.76 ± 194.47	106.43 ± 28.54	17.13 ± 10.64	0.455	0.577
472 ($n = 200$)	193.82 ± 637.75	110.13 ± 27.88	11.32 ± 6.82	0.396	0.485
473 ($n = 200$)	68.18 ± 223.62	102.14 ± 18.99	16.38 ± 10.83	0.881	0.908
474 ($n = 200$)	22.88 ± 47.36	108.35 ± 23.87	15.41 ± 9.51	0.573	0.686
All Patients ($n = 2934$)	47.86 ± 175.63	109.39 ± 24.70	20.52 ± 12.78	0.645 ± 0.19	0.744 ± 0.16